Power Factor Corrector Control Strategies of a Bidirectional Wireless Battery Charger With an Unfolding Active Rectifier

Asier Garcia-Bediaga, *Member, IEEE*, Ander Avila, Itziar Alzuguren, Alex Sanchez, and Alejandro Rujas

***Abstract*— In this article, two power factor corrector (PFC) control strategies for a bidirectional inductive power transfer (IPT) system are proposed. These control strategies are presented for a novel power circuit without input and output interfaces for a wireless electric vehicle battery charger application. This compact topology comprises: unfolding rectifier, primary resonant bridge, and secondary-side active rectification. Two PFC controls are described in detail: a primary-side PFC control, performed in the primary resonant bridge; and a secondary-side PFC control, implemented in the secondary-side active rectification stage. Both strategies are based on a duty-cycle control operating close to the resonance frequency, integrating different functionalities, i.e., PFC, current shaping (CS), and power control on a single control strategy. We analyze each control strategy, evaluating them for different operating points of the charging process. The performance of the wireless charger applying both control strategies is evaluated in terms of power losses, power factor, harmonic distortion, and bifurcation. Additionally, the theoretical results are validated using a GaN-based experimental prototype. The presented analysis and experimental results clearly identify the advantages and limitations of each control strategy leaving no doubt about their usefulness for the future IPT systems.**

***Index Terms*— Electric vehicle, gallium nitride, inductive power transfer (IPT), power factor corrector (PFC).**

I. Introduction

THE development of wide bandgap (WBG) semiconductors along with advanced topology structures have allowed induction power transfer (IPT) technology to become a reality in medium- and high-power applications such as plug-in hybrid and electric vehicles (PHEV/EV) charging systems [1]–[5]. The excellent switching performance of WBG devices and the low-power losses at zero voltage switching (ZVS) operation condition result in power converters with high efficiency and/or high-power density.

Manuscript received 31 August 2021; revised 3 December 2021 and 13 February 2022; accepted 24 March 2022. Date of publication 4 April 2022; date of current version 3 February 2023. This work was supported by the ECSEL Joint Undertaking (JU) through the European Union's Horizon 2020 Research and Innovation Program and Austria, Belgium, Germany, Italy, Norway, Slovakia, Spain, Sweden, and Switzerland, under Grant 826392. Recommended for publication by Associate Editor Martin Ordonez. *(Corresponding author: Asier Garcia-Bediaga.)*

The authors are with the Power Electronics Area, Ikerlan Technology Research Centre, Basque Research and Technology Alliance (BRTA), 20500 Mondragón, Spain (e-mail: agarcia@ikerlan.es).

Color versions of one or more figures in this article are available at https://doi.org/10.1109/JESTPE.2022.3164720.

Digital Object Identifier 10.1109/JESTPE.2022.3164720

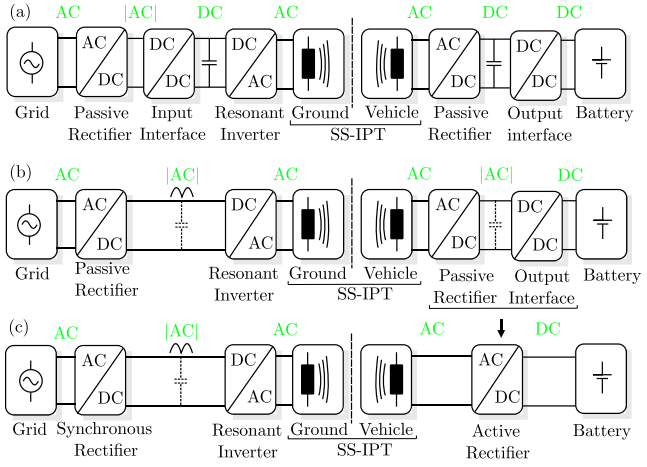

Fig. 1. IPT topologies with different PFC interfaces and power transfer capabilities. (a) Unidirectional power transfer and front-end PFC. (b) Unidirectional power transfer and back-end PFC. (c) Bidirectional power transfer and back-end PFC.

During battery charging process, power factor correction (PFC) and power control from ac to regulated dc output must be provided. In IPT systems, the main tasks of the power conversion system are partitioned/combined in different configurations, as it is analyzed in [6] for solid-state transformers (SSTs). The IPT systems present worse coupling factor than core transformers and a handicap with the required synchronization, communication between primary- and secondary-side converters or parameter estimation methods [7].

IPT circuits are generally based on an input PFC interface [see Fig. 1(a)], also known as a front-end PFC. The input PFC circuits of front-end systems usually require heavy passive components, i.e., inductors and capacitors, with a big impact on the system losses, volume and reliability. Thus, different single-stage topologies with integrated PFC and output power control functionalities have been proposed in the literature [8], [9]. Moreover, performing PFC at the receive side of an IPT system was widely discussed [10]–[12], also known as back-end PFC [see Fig. 1(b)]. Back-end PFC solutions with a single-stage primary circuit present clear advantages in the IPT application. Avoiding the primary-side passive elements directly improves the power density of the power system. Moreover, it reduces the overall cost of the off-board system [12]. However, this circuit adds control

complexity to the on-board converter due to the handicap of the grid synchronization and additional power losses in the output interface. Another drawback of this single-stage solution is the 100 Hz fluctuation power, which increases the root mean square (rms) currents in the primary and secondary coils [12].

Additionally, the automotive industry is currently demanding bidirectional battery chargers, with the enabling the power transfer both in grid-to-vehicle (G2V) and vehicle-to-grid (V2G) operation modes. Different control strategies have been proposed in the literature to control the series–series compensated dc–dc resonant stage of the bidirectional IPT and achieve ZVS, such as dual phase shift (DPS) control [13], triple phase shift (TPS) control [14], or variable-frequency TPS (VFTPS) control [15]. However, these techniques usually require relatively complex synchronization techniques to control the phase shift between primary and secondary bridges. The use of the secondary active rectifier to control the transferred power of IPT systems and to achieve ZVS has been also demonstrated in the literature [16], [17], but in both cases considering unidirectional dc–dc circuits.

Focusing on single-stage ac–dc bidirectional topologies, dual-active-bridge (DAB) with an unfolding rectifier and a high-frequency transformer has been proposed in [18] for an EV plug-in battery charger with unity power factor. Regarding the single-stage back-end PFC circuits for bidirectional IPT systems, the matrix converter with series–series compensation has been analyzed in [19], [20]. Recently, we presented a new single-stage back-end PFC circuit without any intermediate dc-link, with an unfolding rectifier and an active secondary-side rectifier in [21] as an interesting solution for future bidirectional wireless battery chargers [see Fig. 1(c)].

The lack of intermediate energy storage element in the primary side has a direct impact on the current and transferred power, resulting in a twice per grid period fluctuating power flow to the secondary and consequently to the battery [see Fig. 2]. However, experimental results of battery performance evaluations conclude that the effects of low frequency ripple are minimal, appearing as a suitable alternative for dc charging of EV [22].

Fig. 2 presents a detailed schema of the bidirectional back-end PFC with active secondary-side rectifier topology presented in Fig. 1(c). Compared to the work presented in [12], the primary input and secondary passive rectifiers have been replaced by active semiconductors with the main goal of including bidirectionality. The primary active rectifier is now synchronized with the grid voltage to reduce the conduction losses. There is no primary dc-link voltage control, and the resonant inverter is fed by a rectified voltage (|ac|). Commonly, CS and power control are performed on input and/or output interfaces of wireless chargers. However, there is no possibility to implement commonly used PFC control strategies in the novel bidirectional back-end PFC, since there is no input or output interfaces and/or controlled dc-link voltages [21]. Thus, the PFC and (CS) tasks need to be carried out in the resonant inverter or in the secondary active rectifier.

The main motivation of this work is to propose two new PFC control strategies for the novel single-stage back-end circuit, performing in both cases the PFC within the resonant IPT converter, in the primary side or in the secondary side. The main goal of the article is to evaluate the performance of the IPT system applying both control strategies, focusing on the power losses, input total harmonic distortion (THD), efficiency and the bifurcation phenomena.

This work is organized as follows. Section II presents the main concepts of the two novel PFC control strategies. In Section III, a performance evaluation of the proposed topology is presented, comparing the proposed PFC control in the primary and in the secondary sides. Moreover, with the aim of validating this study, experimental measurements with a GaN-based prototype are presented in Section IV. Finally, Section V draws some conclusions.

II. PFC Control Strategies for a Bidirectional Back-End IPT System

One of the most important parameters in IPT systems is the coupling factor, which depends on the constructive parameters of coils, distance between both coils and their misalignment. The coupling factor also defines the relation between the self and mutual inductance:

$$k = \frac{M}{\sqrt{L_{\mathrm{p}} L_{\mathrm{s}}}} \tag{1}$$

where M is the mutual inductance, and L_p and L_s are the self-inductance of primary and secondary coils, respectively.

Considering the relation between primary induced voltage and secondary current, and secondary induced voltage and primary current, the output power at resonance frequency is obtained with (2), for dc–dc operation with square modulation at resonant inverter [23]

$$P = \frac{8}{\pi^2} \frac{V_2\ V_1}{\omega_{\mathrm{o}} M} \tag{2}$$

where ω_o is the resonance pulsation, and V_1 and V_2 are the dc voltages of primary and secondary buses.

It is noteworthy that the frequency control is not considered since the automotive SAE standard J2954 proposes a frequency band between 81.39 and 90 kHz. Thus, the switching frequency is set constant close to the resonance frequency, and it is not employed as a control parameter. Moreover, unlike what is usual in the literature where power is controlled with the primary (v_r) and secondary dc-link (V_{BAT}) voltages, in this work the bidirectional topology is controlled modulating primary (v_p) and/or secondary (v_s) voltages with the corresponding duty cycles of the switching devices (see Fig. 2). Therefore, the power control is achieved regulating the low-frequency mean value of the primary voltage v_{pf} or secondary voltage v_{sf}, and the PFC is ensured with a 100 Hz fluctuating power. With the aim of calculating the feed-forward controls and fundamental voltage references, the duty-cycle expressions are defined in this section. Knowing that a PFC control is desired and considering the lack of any low-frequency storage element, the transferred power has to include the 100 Hz fluctuating power

$$p = v_{\mathrm{grid}} i_{\mathrm{grid}} = P_{\mathrm{mean}} \left(1 + \cos\left(2\omega_{\mathrm{g}} t\right)\right). \tag{3}$$

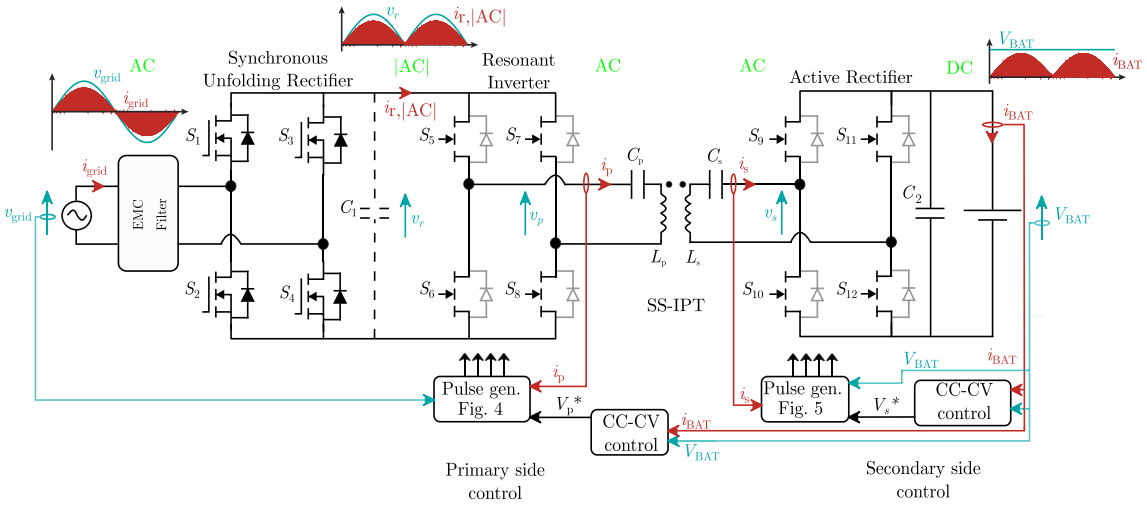

Fig. 2. Analyzed power electronic circuit of the bidirectional single-phase back-end PFC topology, showing control variants and key waveforms.

In this work, we will consider that the battery power control is based on constant current (CC) and constant voltage (CV) control and it will be implemented based on the battery voltage and current measurements. An external battery floating voltage controller is implemented to calculate the battery current reference, and a current saturation is included to achieve the CC control. The internal current control loop assures a correct current regulation, compensating any internal or external perturbation.

Considering that secondary-side voltage is always in phase with the secondary-side resonant current, the transferred power is reformulated as

$$p = \frac{\hat{v_{\mathrm{pf}}}\ \hat{v_{\mathrm{sf}}}}{2\omega_{\mathrm{o}} M} \tag{4}$$

where $\hat{v_{\mathrm{pf}}}$ and $\hat{v_{\mathrm{sf}}}$ are the amplitudes of the primary- and secondary-side fundamental voltages in the switching frequency, which are defined as follows:

$$\hat{v_{\mathrm{pf}}} = \frac{4}{\pi} v_r \sin\left(\delta_{\mathrm{p}}\pi/2\right) \tag{5}$$

$$\hat{v_{\mathrm{sf}}} = \frac{4}{\pi} V_{\mathrm{BAT}} \sin\left(\delta_{\mathrm{s}}\pi/2\right) \tag{6}$$

where δ_p is primary duty cycle, δ_s is secondary duty cycle, V_{BAT} is the battery voltage, and v_r is the grid-rectified voltage

$$v_{\mathrm{r}} = \left|v_{\mathrm{grid}}\right| = V_{\mathrm{grid}} \left|\sin\left(\omega_{\mathrm{g}} t\right)\right| \tag{7}$$

being V_{grid} the grid voltage amplitude and ω_g the grid pulsation.

Thus, two different PFC control strategies can be implemented depending on which converter is performing PFC and CS: the primary-side resonant inverter or the secondary active rectifier. In both control strategies, an unfolding 50 Hz active rectifier is connected to the grid. Thus, an unregulated |ac| voltage supplies the resonant inverter, as it is depicted in Fig. 2. The resonant inverter is modulated to excite primary resonant tank (v_p) and transfer current from primary to secondary coil. Additionally, if the power control is performed in the primary-side resonant inverter (off-board), a communication system or estimation techniques will be required to know in real time the battery voltage and current. Otherwise, this handicap can be avoided with the secondary-side (on-board) control strategy. Hereafter, the main differences of both control strategies are described which are mainly related to the feed-forward control and pulse generation of the resonant inverter and active rectifier.

A. Primary-Side Control

With the aim of controlling the battery charging process with the primary-side control, the primary voltage v_p is modulated while secondary-voltage v_s remains uncontrolled, as it is depicted in Fig. 3(a). A duty-cycle control is proposed in the primary-side resonant inverter using phase shift modulation (PSM). All transistors are commanded with a square modulation and the duty-cycle δ_p is controlled with the phase between both inverter branches. The secondary side can operate as a passive rectifier or synchronized with the resonant current to reduce conduction losses, producing in both cases a constant-amplitude primary current [see Fig. 3(a)].

Fig. 4 shows the feed-forward and the pulse generation of the primary-side control, considering both G2V and V2G operation. The main difference between the two operation modes is related to the pulse generation as both operation modes use the same duty-cycle calculation. Additionally, pulse patterns of each switching device are included differing between switches that switch at the line frequency f_g and the ones that operate at switching frequency f_s (see Fig. 4).

The control concepts are very similar for any power direction, and only few control details have to be considered. For G2V and V2G operation, the primary coil current can be assumed as a constant-amplitude sinus, and therefore the fluctuating power has to be achieved with the primary voltage. Using (3) and (4), the primary-side fundamental voltage reference is defined with

$$\begin{aligned}\hat{v_{\mathrm{p}}^{*}} &= V_{\mathrm{p}}^{*}\left(1+\cos\left(2\omega_{\mathrm{g}} t\right)\right) \\ &= \frac{P_{\mathrm{mean}}^{*} M \omega_{\mathrm{o}} \pi}{2 V_{\mathrm{BAT}}}\left(1+\cos\left(2\omega_{\mathrm{g}} t\right)\right)\end{aligned} \tag{8}$$

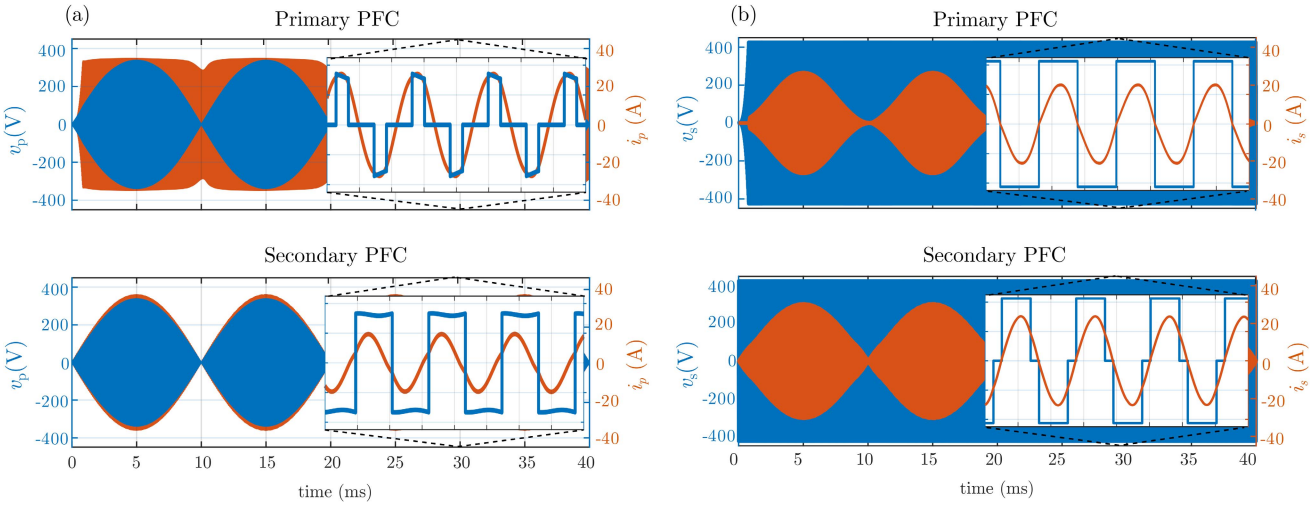

Fig. 3. Waveforms with PFC control in the primary resonant inverter (primary PFC) and in the secondary side (secondary PFC). (a) Primary-side voltage (v_p) and current (i_p). (b) Secondary-side voltage (v_s) and current (i_s).

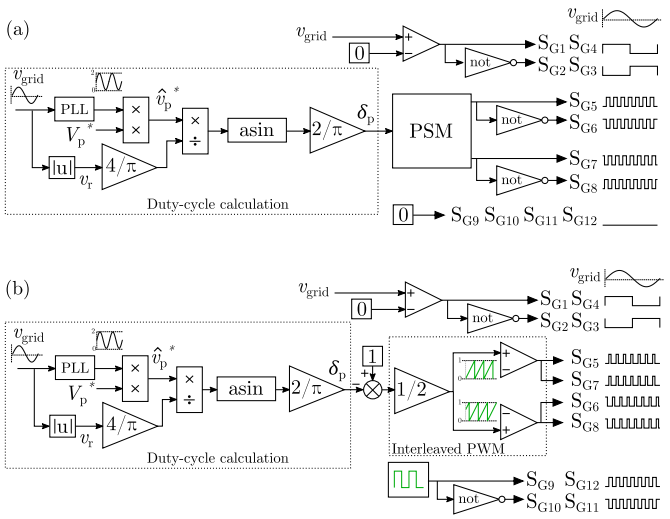

Fig. 4. Primary-side control strategy, which is composed of duty-cycle calculation (δ_p) and pulse generation of different stages: unfolding rectifier (S_{G1}, S_{G2}, S_{G3}, S_{G4}), resonant inverter (S_{G5}, S_{G6}, S_{G7}, S_{G8}) and active rectifier (S_{G9}, S_{G10}, S_{G11}, S_{G12}). This control strategy is presented for different operation modes (a) G2V and (b) V2G operation.

where the cosine waveform can be deduced using a phase-locked loop (PLL) from the grid voltage measurement and the M/V_{BAT} can be estimated using the peak measurement of primary-side coil current

$$\frac{M}{V_{BAT}} = \frac{4}{\pi\,\omega_o \hat{i_p}}. \tag{9}$$

From the primary-side steady-state measurement, it is not straightforward to extract M and V_{BAT} separately, since both parameters have a relatively large range, and communication or other estimation techniques could be necessary to have a precise V_{BAT} estimation.

Hence, using (5) the primary-side duty cycle can be calculated with the following expression:

$$\delta_p = \frac{2}{\pi}\arcsin\left(\frac{\pi\,\hat{v_p^*}}{4v_r}\right). \tag{10}$$

B. Secondary-Side Control

In the secondary-side control strategy, a δ_s duty-cycle control is implemented in the secondary rectifier using an interleaved pulsewidth modulation (PWM). In this control strategy, the voltage of secondary side is modulated, achieving a variable amplitude primary current, and the inverter can be operated with an uncontrolled square-wave modulation, as it is shown in Fig. 3(b). Although the phase of the carrier signal of secondary-side modulation affects the transferred power and power losses, as it is explained in [13], [16], [17], this work does not go into detail to analyze this degree of freedom.

In this case, assuming that the on-board system does not have the grid voltage measurements to implement a PLL, the secondary coil current amplitude values can be used as PLL input to achieve the low-frequency sinusoidal waveform. Thus, the secondary voltage reference should be

$$\hat{v_s^*} = V_s^*\left|\sin\left(\omega_g t\right)\right| = \frac{P_{mean}^* M \omega_o \pi}{V_{grid}}\left|\sin\left(\omega_g t\right)\right| \tag{11}$$

where M/V_{grid} value can be estimated from the secondary peak current value (7) and (12), since it is not straightforward to obtain both variables separately. However, in this case, the range of the grid voltage amplitude is relatively limited, and then, a good estimation of coupling factor is possible

$$\frac{M}{v_r} = \frac{4}{\pi\,\omega_o \hat{i_s}}. \tag{12}$$

Then, substituting (6) the secondary-side duty cycle can be calculated with

$$\delta_s = \frac{2}{\pi}\arcsin\left(\frac{\pi\,\hat{v_s^*}}{4V_{BAT}}\right). \tag{13}$$

The feed-forward, i.e., δ_s calculation, is similar for both operation modes (G2V and V2G), as it is shown in Fig. 5. Besides, pulse patterns of each switching device are included differing between switches that switch at the line frequency f_g and the ones that operate at switching frequency f_s (see Fig. 5).

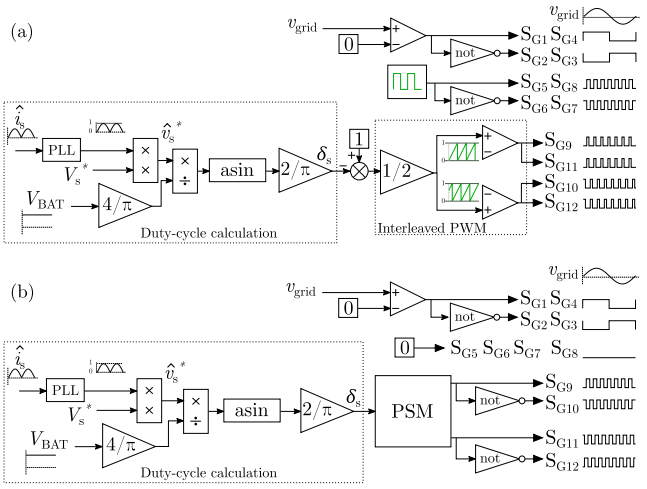

Fig. 5. Secondary-side control strategy, which is composed of duty-cycle calculation (δ_s) and pulse generation of different stages: unfolding rectifier (S_{G1}, S_{G2}, S_{G3}, S_{G4}), resonant inverter (S_{G5}, S_{G6}, S_{G7}, S_{G8}) and active rectifier (S_{G9}, S_{G10}, S_{G11}, S_{G12}). This control strategy is presented for different operation modes (a) G2V and (b) V2G operation.

TABLE I
SPECIFICATIONS AND PARAMETERS OF CONTACTLESS BATTERY CHARGER

Description	Variable	Value	Unit
Output power	P_{out}	3.6	kW
Input voltage	$V_{in,ac}$	230	V_{RMS}
Output voltage	$V_{out,dc}$	250-425	V
Resonance frequency	f_o	85	kHz
Coupling factor	k	0.2-0.4	
Primary coil inductance	L_p	116	μH
Secondary coil inductance	L_s	116	μH
Primary resonant capacitor	C_p	31	nF
Secondary resonant capacitor	C_s	31	nF

III. PERFORMANCE EVALUATION

In this section, the performance of the IPT system for the proposed control strategies is evaluated, considering the specifications and parameters presented in Table I.

The performance of the proposed control strategies and the power converter depends on different design parameters and operation conditions. This evaluation considers the analysis of a designed IPT system, whose main parameters are presented in Table I, and it studies the influence of the coupling factor k, operating points (see Fig. 6) and switching frequency.

A. Bifurcation

The bifurcation is one of the most important design aspects to consider in the IPT systems, since it defines the switching modes depending on the frequency-dependent load impedance of the resonant inverter. This resonant inverter can operate in the inductive region, with ZVS; in the resistive region, with ZCS or in the capacitive region with hard-switching. Therefore, the bifurcation can have a big impact on the system performance, specially in the power losses of semiconductors and, consequently, on the system efficiency.

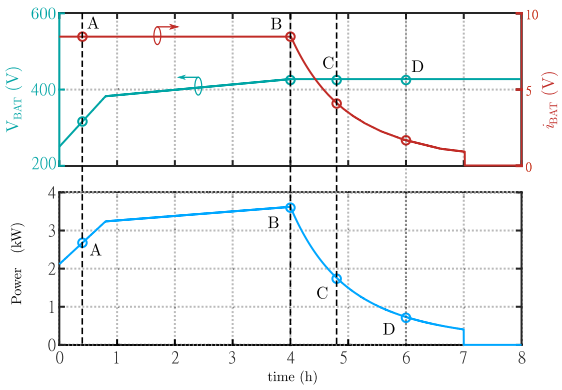

Fig. 6. Different operation points of the wireless charger considering a full charging profile.

The bifurcation conditions are widely discussed in the literature, and generally designers try to avoid this phenomena with the design of the coils and the resonant compensation based on the operating conditions. There are several parameters that can be considered to avoid bifurcation, such as the ratio of coil self-inductances, the coupling factor, the transferred power or the compensation capacitor [24]. However, depending on the system requirements, it is not always possible to avoid it and the bidirectionality of the system can limit these possibilities.

With the aim of looking for the bifurcation limits, based on [24], the limit expressions have been modified for the analysis of the different duty-control strategies proposed before

$$p_{\text{lim}} = \frac{\hat{v_s}^2}{2\omega_o L_s k} \tag{14}$$

$$k_{\text{lim}} = \frac{\hat{v_s}^2}{2\omega_o L_s p} \tag{15}$$

$$x_{\text{lim}} = \left(\frac{\hat{v_p}}{\hat{v_s}}\right)^2 \tag{16}$$

where x is the ratio of coils inductances, which is defined as

$$x = \frac{L_p}{L_s}. \tag{17}$$

To analyze the bifurcation, the input impedance expression is expanded considering G2V operation

$$Z_{\text{in}} = \frac{\vec{v_p}}{\vec{i_p}} = \frac{\left(\omega^2 M\right)^2 - L_1 L_2 \left(\omega^2 - \omega_o^2\right)^2}{\omega\left(\left(\omega^2 - \omega_o^2\right)^2 L_2^2 + \omega^2 R_{\text{sac}}^2\right)} + \frac{j\omega L_p \left(\omega^2 - \omega_o^2\right) R_{\text{sac}}}{\omega\left(\left(\omega^2 - \omega_o^2\right)^2 L_2^2 + \omega^2 R_{\text{sac}}^2\right)} \tag{18}$$

where the equivalent secondary-side load ac resistance can be calculated as

$$R_{\text{sac}} = \frac{\widehat{v_s}}{\widehat{i_s}}. \tag{19}$$

If primary-side control is implemented, this resistance depends on the output equivalent resistance, and it is defined as follows:

$$R_{\text{sac}} = \frac{\frac{4}{\pi} V_{\text{BAT}}}{\frac{\pi}{2} i_{\text{BAT}}} = \frac{8}{\pi^2} R_{2,\text{dc}}. \tag{20}$$

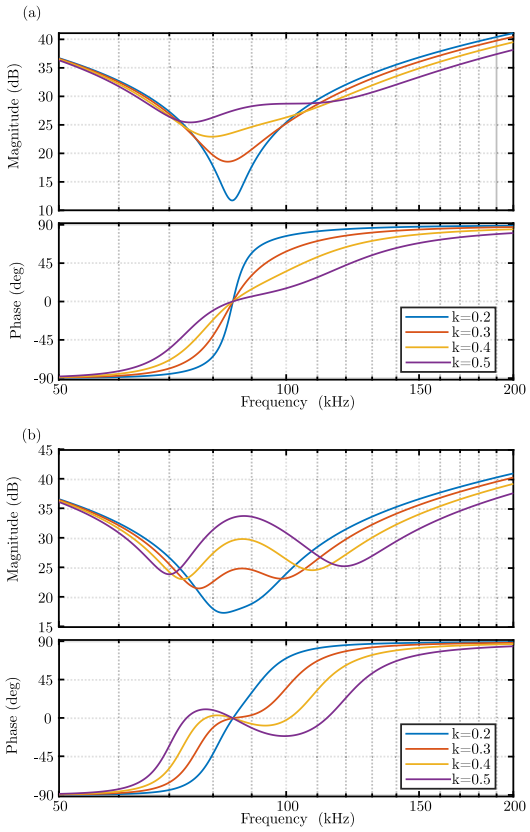

Fig. 7. Bode diagram of input impedance $Z_{\text{in}}\angle\varphi$ for different coupling factors k working in B operating point for different control strategies (a) primary-side control and (b) secondary-side control.

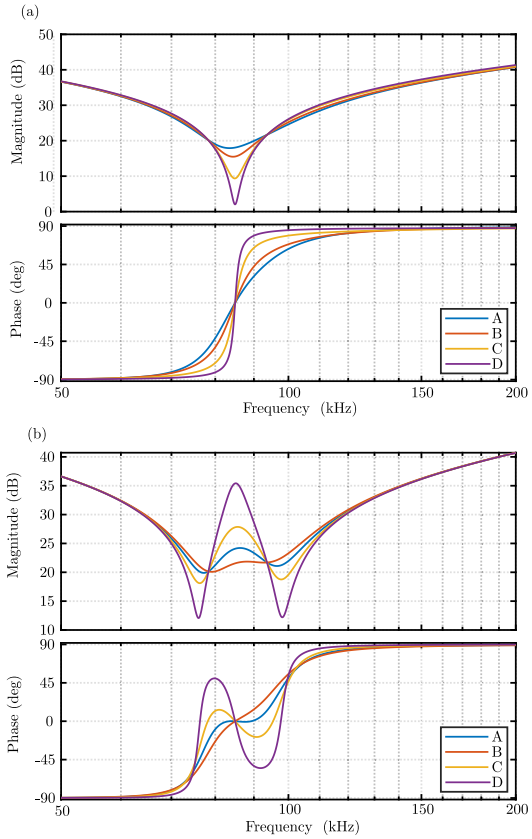

Fig. 8. Bode diagram of input impedance $Z_{\text{in}}\angle\phi$ with $k = 0.25$ for different operating points and control strategies (a) primary-side control and (b) secondary-side control.

On the contrary, with the secondary control strategy, the equivalent ac resistance changes with the duty cycle

$$R_{\text{sac}} = \frac{8}{\pi^2}\frac{V_{\text{BAT}}^2 \sin^2(\delta_s \pi/2)}{p} = \frac{8}{\pi^2} R_{2,\text{dc}} \sin^2(\delta_s \pi/2). \quad (21)$$

The particular case of the input impedance at resonance, (18) is simplified as

$$Z_{\text{in},\ \omega=\omega_o} = \frac{\omega_o^2 k^2 L_p L_s}{R_{\text{sac}}}. \quad (22)$$

In this article, with the aim of simplifying the design of the bidirectional system, a symmetrical hardware design of the IPT resonant compensation has been considered, with identical primary and secondary coils, i.e., unitary coil inductance ratio x, and primary and secondary resonant capacitors tuned to the same resonant frequency, specifically to 85 kHz.

Fig. 7 shows the input impedance bode diagram, with the magnitude in terms of the switching frequency. A positive phase means an inductive operation, and ZVS can be achieved, whereas a negative phase forces capacitive zone and hard-switching operation. Analyzing the bifurcation for the primary-side control in the case study, we can see that for B operating point primary-side control is free of bifurcation, even with high coupling factor values [see Fig. 7(a)]. Nevertheless, secondary-side control presents bifurcation for high coupling factors ($k > 0.3$), as it is shown in Fig. 7(b).

Moreover, the bifurcation is analyzed for a favorable coupling factor of 0.25 and for different operating points (see Fig. 8). In the case of the primary-side control, the bifurcation is avoided for every operating point, as it is shown in Fig. 8(a). However, for the secondary-side control we can say as follows.

1) Power, coupling and voltage ratio are very close to the bifurcation limit for operating point A.
2) Power and coupling are below the limits, and the secondary voltage is higher than primary one, i.e., there is no bifurcation for operating point B.
3) Power and coupling are above the limits, and the secondary voltage is lower than primary one, i.e., there is bifurcation due to the v_s voltage reduction in the CV region for operating point C and D.

Therefore, to avoid the bifurcation for secondary-side control, low values of coupling factors [see Fig. 7(b)], low-power operation points [see Fig. 8(b)] and an emitter voltage $\hat{v_p}$ lower than receiver $\hat{v_s}$ are required.

With the aim of validating the analysis, some simulations have been performed in C operating point (see Fig. 9) with a switching frequency slightly above resonance frequency. It can be seen that, with primary control, the circuit works in inductive zone, whereas a capacitive operation is achieved with the secondary control.

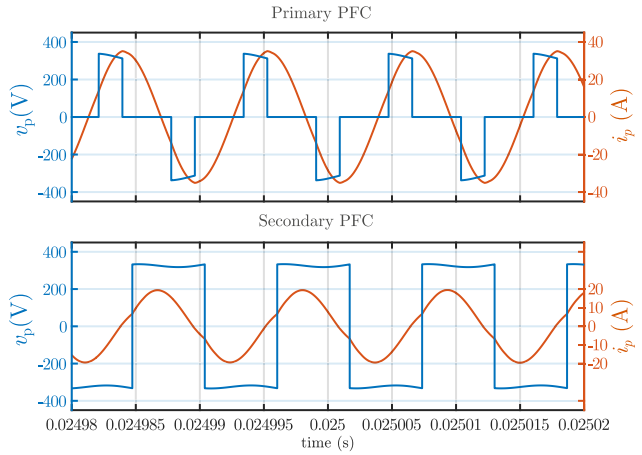

Fig. 9. Primary inverter voltage (v_p) and current (i_p) waveforms with primary-side control and secondary-side control, operating at a switching frequency 104% of resonance.

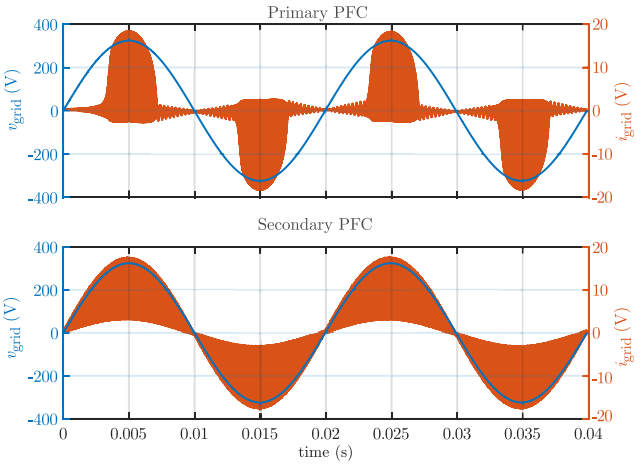

Fig. 10. Grid voltage (v_{grid}) and current (i_{grid}) waveforms with primary PFC control secondary PFC control, operating at a switching frequency 104% of resonance.

B. PFC, THD and Minimum Induced Voltage

The operation close but out of the resonance is typical to ensure enough inductive energy in the resonant tank and to achieve ZVS in the resonant inverter. However, another important consideration of IPT systems with an output CV is the minimum induced voltage in the receiver coil. Iruretagoyena *et al.* compare in [23] the differences between an uncontrolled and a controlled output voltage operation. It concludes that the secondary rectifier can produce a non-linear behavior when switching frequency is not just in resonance, because there is not enough induced voltage to polarize the semiconductor devices. This phenomena is specially critical during the zero-crossing of grid voltage and/or in low load conditions, e.g., in the last part of CV (D point). Hence, the impact on the input current THD of the non-linearity produced by minimum induced voltage is analyzed with the proposed two control strategies.

Fig. 10 shows the grid voltage and current waveforms of both control strategies operating at a switching frequency 104% of resonance. Analyzing the grid current,

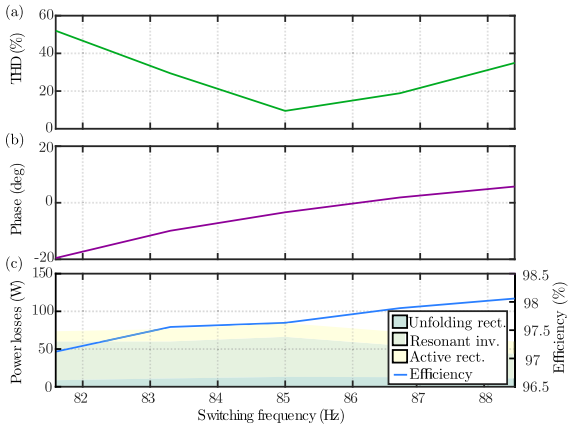

Fig. 11. Primary-side control strategy performance versus switching frequency in B operation point and 0.25 coupling factor. (a) THD of the input current. (b) Primary-side phase. (c) Power losses distribution and efficiency, including semiconductors of unfolding rectifier (S_1, S_2, S_3, S_4), resonant inverter (S_5, S_6, S_7, S_8) and active rectifier (S_9, S_{10}, S_{11}, S_{12}).

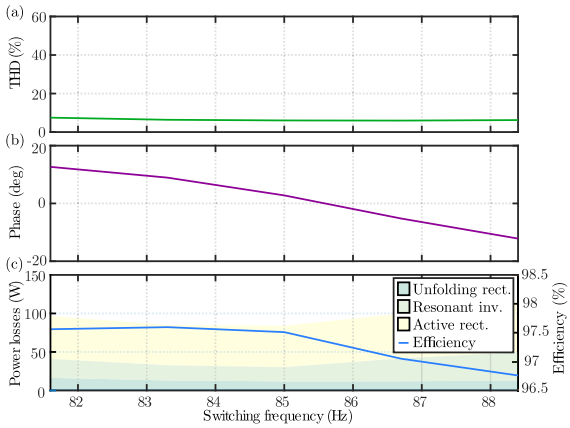

Fig. 12. Secondary-side control strategy performance versus switching frequency in B operation point and 0.25 coupling factor (a) THD of the input current, (b) primary-side phase, and (c) power losses distribution and efficiency, including semiconductors of unfolding rectifier (S_1, S_2, S_3, S_4), resonant inverter (S_5, S_6, S_7, S_8) and active rectifier (S_9, S_{10}, S_{11}, S_{12}).

a higher THD and a higher di/dt can be found in the primary-side control, due to the zero-voltages applied in the inverter. The primary control strategy does not induce enough voltage close to the grid zero-crossing. Thus, there is not an active power transfer and a non-linear behavior of the current is achieved, leading to poor PFC and THD. On the contrary, the secondary-side control operates with a higher primary voltage and smaller secondary voltage in all operation points. Therefore, the non-linearity close to the grid zero-crossing is negligible.

Varying the switching frequency, Fig. 11 illustrates how THD characteristics are clearly improved at resonance frequency with the primary-side control, since the voltage drop in the resonant tank is smaller and, then, higher the induced voltage. On the contrary, the secondary control is hardly affected by going out of resonance, and a relatively low THD is achieved in the analyzed frequency range (see Fig. 12).

C. Power Losses

The power losses breakdown of the bidirectional back-end PFC topology were already presented in [21]. A power losses

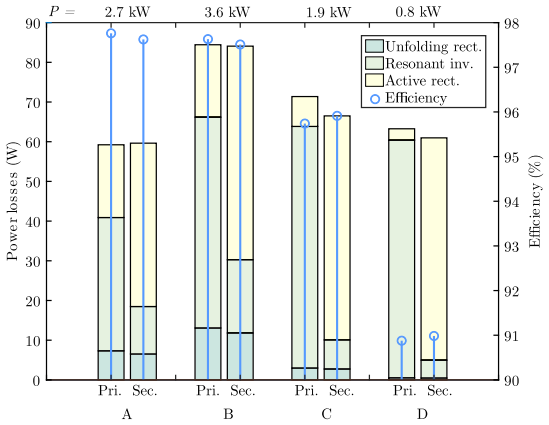

Fig. 13. Power losses of different stages and efficiency performance of both control strategies for different operating points, a switching frequency of 85 kHz, close to the resonance, and low coupling factor ($k = 0.25$).

comparison is carried out in this section considering the case study presented in Table I. For this analysis only power semiconductors losses are considered, as different control strategies mainly affect to the semiconductors of the power converter. First, the analysis has been carried out in terms of the switching frequency, as it is depicted in Figs. 11 and 12. Primary control operates without bifurcation and a higher efficiency is achieved above resonance frequency due to ZVS and reduction of inverter power losses. On the contrary, the secondary-side control has bifurcation, and that is why, better efficiency characteristic is achieved below resonance frequency. Operation close to the optimal switching frequency is relatively simple in no bifurcated systems, since the input impedance of the load is always inductive above the resonant frequency, achieving ZVS, as with the primary-side control strategy.

Fig. 13 summarizes the power losses in each stage and the efficiency performance of the system, only considering the power losses of the semiconductors. It has to be noted that, as it was previously mentioned, the carrier signal has been considered in phase with the secondary-side current, producing turn-on and turn-off losses on the secondary rectifier. Moreover, the switching frequency is close to the resonance, avoiding the bifurcation effect of secondary-side control. The efficiency results show that both control strategies presents similar power losses but differently distributed, as it was expected due to different switching patterns presented in Figs. 4 and 5.

D. Summary and Discussion

Table II compares the performance of the studied IPT system for the proposed control strategies. We can conclude that primary control is much more robust to avoid the bifurcation in G2V operation. Besides, regarding THD and PFC, the presented analysis conclude that the secondary-side control is more robust to achieve PFC operation than the primary-side control in G2V operation. This is mainly due to the non-linearity produced by the minimum induced voltage for the primary-side control. In terms of power losses, similar power losses are achieved operating close to resonance frequency, but differently distributed (see Fig. 13).

Primary-side control achieves low power losses when operating in the inductive zone, with ZVS. However, operation out of the resonance during the zero-crossing instants reduces considerably its THD performance. A possible technical solution to ensure ZVS in the primary-side control and PFC is with a variable switching frequency control depending on the grid voltage, approaching to resonance frequency in zero-crossing instants. However, it could increase the complexity of the software implementation. Moreover, switching sequence aside, there is a clear conclusion that the secondary rectifier losses are much lower than in the secondary-side control, and this effect can be explained since the voltage of secondary side is higher, and thus, lower current has to be managed and lower conduction losses can be expected.

For the secondary-side control, it is more complex to ensure ZVS due to bifurcation. However, if the system has bifurcation, and the optimal switching frequency is desired, a real-time phase estimator and adaptive frequency control could be needed, increasing the complexity of the software implementation. Regarding the switching losses of secondary rectifier, as [17] describes for a dc–dc IPT, the advantage of the secondary-side control is that a full ZVS and ZCS can be achieved with a controlled secondary active rectifier if transistors gates are correctly synchronized.

All these conclusions in terms of bifurcation, THD, PFC and power losses can follow the same path for V2G but all in reverse. In this case, the resonant inverter and active rectifier roles are swapped, and so do gate generation of the primary and secondary control algorithms. However, since in this work a symmetrical IPT system has been employed, i.e., similar voltage and coil inductance values, the conclusions in terms of efficiency and implementation are the same as for G2V. A negligible non-linearity behavior is found with primary-side PFC control in V2G, being easier to ensure a correct THD and PFC performance. However, as the power flow is inverse, bifurcation and power losses challenge can be found with the primary-side PFC control in V2G.

Therefore, designer has to decide the trade-off and what is better solution in terms of bifurcation, THD, PFC and power losses (see Table II) depending on its system requirements and the power direction. Usually, optimize as much as possible the on-board converter to reduce the stress and minimize its cooling requirement can be a logical decision in PHEV/EV IPT applications, while limiting the coupling factor to avoid bifurcation.

IV. Experimental Validation

This section presents the experimental validation of previously presented concepts. The experimental platform is formed by the power branches depicted in Fig. 14(a) and the height (Z) adjustable platform that includes the emitter and receiver coil inductors [see Fig. 14(b)]. For the PCB design, GaN transistors (IGO60R070D1) and SiC diodes (C5D50065D) have been considered with the aim of validating the unidirectional and bidirectional configurations. This PCB is the same for all converter branches of the configuration

TABLE II
IPT SYSTEM PERFORMANCE EVALUATION FOR DIFFERENT CONTROL STRATEGIES IN G2V OPERATION

	Bifurcation	THD	PFC	Power losses
Primary PFC	Non-bifurcated	• Variable • Low close to ω_0	Medium **	• Resonant inverter stress • ZVS operation
Secondary PFC	Bifurcated*	Low	High	• Active rectifier stress • Complex ZVS operation

* Operating at low power and/or high coupling factor (k >0.3).
** Due to the non-linearity produced by the required minimum induced voltage.

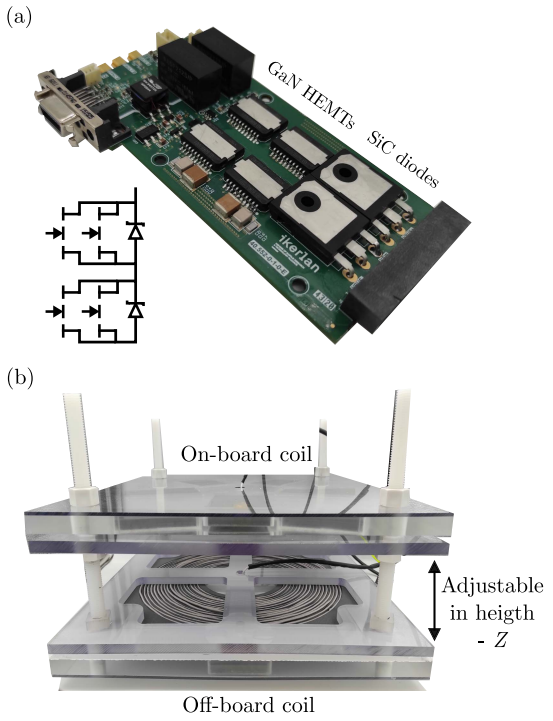

Fig. 14. Experimental IPT system for the validation of the concepts (a) GaN devices with anti-parallel SiC diodes and (b) on-board and off-board coils, fabricated on an in height adjustable platform.

TABLE III
CHARACTERISTICS OF THE INDUCTIVE COILS

Description	Value	Unit
Coil diameter	320	mm
Wire	Litz 1440x0.07	
Ferrite core	3C95 20x PLT64/50/5	
Transmission frequency - f_o	85	kHz
Coupling coefficient - k	0.22	
Distance- Z	100	mm
Primary inductance- L_p	120	μH
Secondary inductance- L_s	120	μH

presented in Fig. 2. The characteristics of inductive coils of the experimental set-up are described in Table III.

To validate that secondary-side control strategy is more prone to bifurcation phenomena, a frequency sweep has been done for both control strategies. Fig. 15 shows how for primary-side control strategy, the circuit is in inductive zone, above the resonant frequency ($\varphi = 42°$), while a capacitive

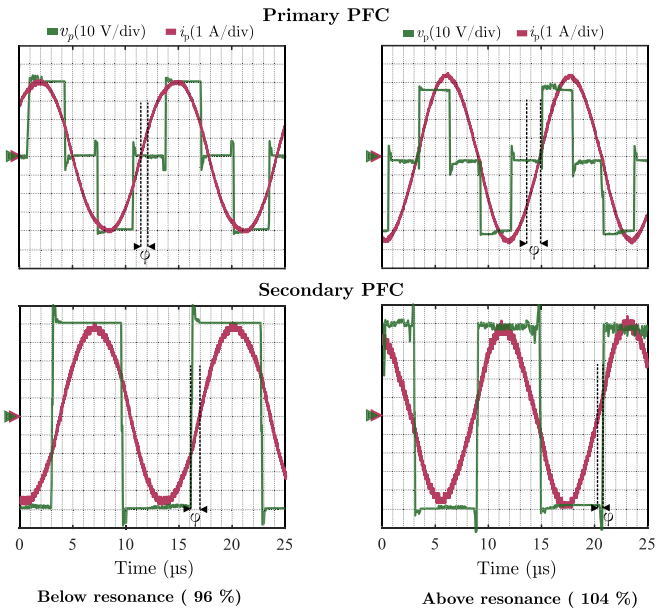

Fig. 15. Primary-side high-frequency voltage and current waveforms with primary and secondary control strategies. Operation below resonant frequency (left) and above resonance (right).

operation is clearly distinguishable bellow the resonant frequency ($\varphi = -22°$). Conversely, the opposite tendency occurs in the case of the secondary-side control, with a phase of $-22°$ and 25° for above and bellow operation, respectively. These results clearly validate the bifurcation phenomena analyzed before.

Regarding to the PFC, THD and minimum induced voltage, secondary-side control strategy is the best suited for PFC operation. With primary-side control, non-linearity problems occur when going off-resonance, resulting in a loss of the input current wave quality (see Fig. 16).

With the aim of comparing THD, efficiency and PF values, both control strategies have been evaluated at different operation frequencies. The total power factor is calculated from the distortion power factor and the displacement power factor. However, in all measurements, the displacement power factors are near to the unitary value, and the power factor mainly depends on the distortion power factor, i.e., THD value.

As Fig. 17 shows, experimental measurements verify that the secondary-side control achieves a quasi-constant THD around 8% for any operation frequency (a power factor above 0.99) and a minimum value of 6% THD. Whereas, the primary-side control depends on the operation frequency

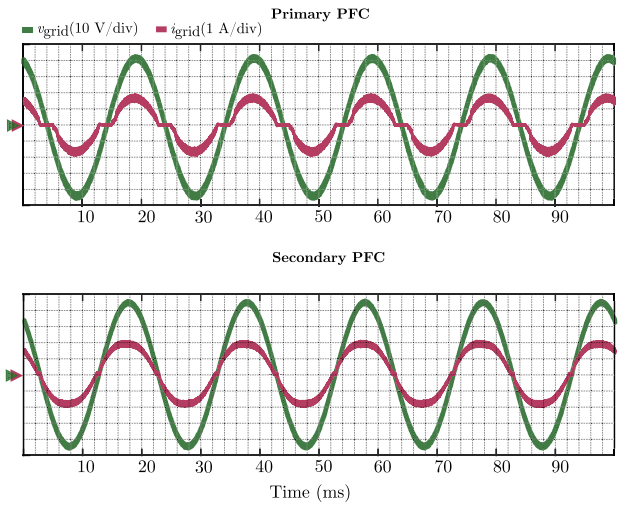

Fig. 16. Low-frequency input voltage and current waveforms. Primary-side PFC control (above) and secondary-side PFC control (below).

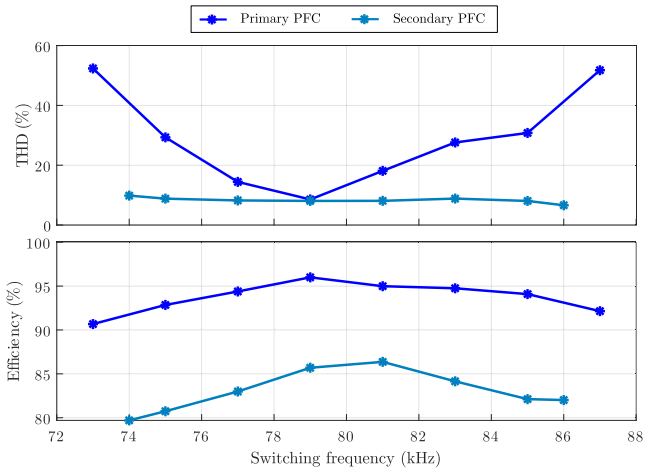

Fig. 17. Experimental THD and efficiency measurements of the proposed two PFC control strategies.

and only reaches a THD below 10% and a power factor above 0.99 near the resonance frequency, i.e., 79 kHz in laboratory set-up. These experimental results validate the simulation tendencies presented in Section III and the effectiveness of the proposed methods.

Regarding the efficiency, the experimental measurements of Fig. 17 consider all the system losses, i.e., not only the converter power losses but also the losses produced by passive elements like the inductive coils. High efficiency values are achieved with the primary-side control, being minimal the impact of the duty-cycle control on power losses. In the case of the secondary-side control, the efficiency is considerably reduced since ZVS condition is not being assured. Achieve ZVS condition in the secondary-side control is more complex, but it is feasible if all transistors gates are synchronized to the secondary-side ac current.

V. Conclusion

This article proposes two different control strategies for a bidirectional back-end PFC topology, without any input or output interface stages. The implementation of the bidirectional back-end PFC topology results in a compact and low-weight power converter in comparison to conventional solutions, but increasing the complexity of the control. Within this context, two control strategies are proposed and analyzed. These control strategies are based on a duty-cycle control of the resonant stage, performing power control and PFC in primary side or in the secondary side. Both control strategies are described in detail along with a performance evaluation of each control option. The performance of the IPT system is evaluated for different operating conditions to identify the advantages of each control strategy. Both alternatives are compared in terms of power losses, harmonic distortion and bifurcation. Primary-side control has demonstrated a higher efficiency than secondary-side control but with higher harmonic distortion. Besides, secondary-side control presents bifurcation depending on the operating point, while the primary-side control results on a non-bifurcated system for every operating point. In addition, theoretical evaluation results were experimentally validated, showing the benefits and limitations of each control strategy.

Acknowledgment

This work was supported by the ECSEL Joint Undertaking (JU) through the European Union's Horizon 2020 Research and Innovation Program and Austria, Belgium, Germany, Italy, Norway, Slovakia, Spain, Sweden, and Switzerland, under Grant 826392.

References

[1] G. A. Covic and J. T. Boys, "Modern trends in inductive power transfer for transportation applications," *IEEE J. Emerg. Sel. Topics Power Electron.*, vol. 1, no. 1, pp. 28–41, Mar. 2013.

[2] M. Chinthavali, O. C. Onar, S. L. Campbell, and L. M. Tolbert, "Integrated charger with wireless charging and boost functions for PHEV and EV applications," in *Proc. IEEE Transp. Electrific. Conf. Expo. (ITEC)*, Jun. 2015, pp. 1–8.

[3] R. Bosshard and J. W. Kolar, "All-SiC 9.5 kW/dm^3 on-board power electronics for 50 kW/85 kHz automotive IPT system," *IEEE J. Emerg. Sel. Topics Power Electron.*, vol. 5, no. 1, pp. 419–431, Mar. 2017.

[4] A. Q. Cai and L. Siek, "A 2-kW, 95% efficiency inductive power transfer system using gallium nitride gate injection transistors," *IEEE J. Emerg. Sel. Topics Power Electron.*, vol. 5, no. 1, pp. 458–468, Mar. 2017.

[5] S. Jayalath and A. Khan, "Design, challenges, and trends of inductive power transfer couplers for electric vehicles: A review," *IEEE J. Emerg. Sel. Topics Power Electron.*, vol. 9, no. 5, pp. 6196–6218, Oct. 2021.

[6] J. E. Huber, D. Rothmund, and J. W. Kolar, "Comparative evaluation of isolated front end and isolated back end multi-cell SSTs," in *Proc. IEEE 8th Int. Power Electron. Motion Control Conf. (IPEMC-ECCE Asia)*, May 2016, pp. 3536–3545.

[7] Y. Liu, U. K. Madawala, R. Mai, and Z. He, "Primary-side parameter estimation method for bidirectional inductive power transfer systems," *IEEE Trans. Power Electron.*, vol. 36, no. 1, pp. 68–72, Jan. 2021.

[8] H. Nazi, E. Babaei, S. Tohidi, and M. Liserre, "Design and analysis of an isolated single-stage resonant AC–DC converter with PFC," in *Proc. 12th Power Electron., Drive Syst., Technol. Conf. (PEDSTC)*, Feb. 2021, pp. 1–5.

[9] C. Wang, S. Pan, and P. Jain, "A 380 V AC–DC single stage three level resonant converter without auxiliary circuit," in *Proc. IEEE Int. Telecommun. Energy Conf. (INTELEC)*, Oct. 2015, pp. 1–6.

[10] J. T. Boys, C.-Y. Huang, and G. A. Covic, "Single-phase unity power-factor inductive power transfer system," in *Proc. IEEE Power Electron. Spec. Conf.*, Jun. 2008, pp. 3701–3706.

[11] G. R. Kalra, D. J. Thirmawithana, M. Neuburger, B. Riar, U. K. Madawala, and R. Zane, "A novel boost active bridge based wireless power interface for V2G/G2 V applications," in *Proc. IEEE Southern Power Electron. Conf. (SPEC)*, Dec. 2017, pp. 1–6.

[12] A. Avila, A. Garcia-Bediaga, U. Iruretagoyena, I. Villar, and A. Rujas, "Comparative evaluation of front- and back-end PFC IPT systems for a contactless battery charger," *IEEE Trans. Ind. Appl.*, vol. 54, no. 5, pp. 4842–4850, Oct. 2018.
[13] T. Diekhans and R. W. D. Doncker, "A dual-side controlled inductive power transfer system optimized for large coupling factor variations and partial load," *IEEE Trans. Power Electron.*, vol. 30, no. 11, pp. 6320–6328, Nov. 2015.
[14] X. Zhang, T. Cai, S. Duan, H. Feng, H. Hu, J. Niu, and C. Chen, "A control strategy for efficiency optimization and wide ZVS operation range in bidirectional inductive power transfer system," *IEEE Trans. Ind. Electron.*, vol. 66, no. 8, pp. 5958–5969, Aug. 2019.
[15] Y. Liu, U. K. Madawala, R. Mai, and Z. He, "An optimal multivariable control strategy for inductive power transfer systems to improve efficiency," *IEEE Trans. Power Electron.*, vol. 35, no. 9, pp. 8998–9010, Sep. 2020.
[16] K. Colak, E. Asa, M. Bojarski, D. Czarkowski, and O. C. Onar, "A novel phase-shift control of semibridgeless active rectifier for wireless power transfer," *IEEE Trans. Power Electron.*, vol. 30, no. 11, pp. 6288–6297, Nov. 2015.
[17] T. Mishima and E. Morita, "Comparative evaluation of secondary-side ZVS-PWM controlled GaN-HFET resonant converters for inductive power transfer," in *Proc. IEEE Energy Convers. Congr. Expo. (ECCE)*, Oct. 2017, pp. 2610–2617.
[18] J. Everts, F. Krismer, J. Van den Keybus, J. Driesen, and J. W. Kolar, "Optimal ZVS modulation of single-phase single-stage bidirectional DAB AC–DC converters," *IEEE Trans. Power Electron.*, vol. 29, no. 8, pp. 3954–3970, Aug. 2014.
[19] S. Weerasinghe, U. K. Madawala, and D. J. Thrimawithana, "A matrix converter-based bidirectional contactless grid interface," *IEEE Trans. Power Electron.*, vol. 32, no. 3, pp. 1755–1766, Mar. 2017.
[20] M. Moghaddami and A. I. Sarwat, "Single-phase soft-switched AC–AC matrix converter with power controller for bidirectional inductive power transfer systems," *IEEE Trans. Ind. Appl.*, vol. 54, no. 4, pp. 3760–3770, Jul. 2018.
[21] A. Sanchez, A. Garcia-Bediaga, I. Alzuguren, I. Zubitur, and A. Rujas, "An ultra-low weight bidirectional back-end PFC topology," in *Proc. IEEE Energy Convers. Congr. Expo. (ECCE)*, Oct. 2021, pp. 1224–1229.
[22] T.-H. Kim *et al.*, "Analytical study on low-frequency ripple effect of battery charging," in *Proc. IEEE Vehicle Power Propuls. Conf.*, Oct. 2012, pp. 809–811.
[23] U. Iruretagoyena, A. Garcia-Bediaga, A. Rujas, H. Camblong, and I. Villar, "Operation boundaries of single/three phase inductive power transfer systems with series-series compensation," in *Proc. 19th Eur. Conf. Power Electron. Appl. (EPE ECCE Eur.)*, Sep. 2017, p. 1.
[24] U. Iruretagoyena, A. Garcia-Bediaga, L. Mir, H. Camblong, and I. Villar, "Bifurcation limits and non-idealities effects in a three-phase dynamic IPT system," *IEEE Trans. Power Electron.*, vol. 35, no. 1, pp. 208–219, Jan. 2020.

Asier Garcia-Bediaga (Member, IEEE) received the B.Sc. degree in electronics from the University of Mondragón, Mondragón, Spain, in 2007, the M.Sc. degree from the Electrical, Electronics, Computer Science, Hydraulics and Telecommunications Engineering School (ENSEEIHT), Toulouse, France, in 2009, and the Ph.D. degree from the Swiss Federal Institute of Technology Lausanne (EPFL), Lausanne, Switzerland, in 2014.

Since 2014, he has been with the Ikerlan Technology Research Centre, Mondragón, as a Researcher in power electronics area. His research interests include wide bandgap power electronics devices and the design, control and optimization of hard and soft-switching power converters for railway, renewable energy, storage systems, and inductive power transfer applications.

Ander Avila received the B.Sc. degree in industrial electronics and the M.Sc. degree in energy and power electronics from the University of Mondragón, Mondragón, Spain, in 2013 and 2015, respectively. He is currently pursuing the Ph.D. degree in collaboration with the Ikerlan Technology Research Centre, Mondragón, and the Power Supply System Group, University of Oviedo, Gijón, Spain.

Since 2015, he has been a Researcher with the Ikerlan Technology Research Centre. His current research interests include the design and optimization of power converters for electrical traction, renewable energy, inductive power transfer, and energy storage applications, based on wide bandgap devices.

Itziar Alzuguren received the B.S. degree in energy engineering from the University of Mondragón, Mondragón, Spain, in 2019, and the M.Sc. degree in industrial electronics from the Universidad Politécnica de Madrid (UPM), Madrid, Spain, in 2020. She is currently pursuing the Ph.D. degree in collaboration with the Ikerlan Technology Research Centre, Mondragón, and the Centro de Electrónica Industrial (CEI), UPM.

Since 2020, she has been a Researcher with the Ikerlan Technology Research Centre. Her current research interests include the design and optimization of power converters for electrical traction, renewable energy, inductive power transfer, and energy storage applications, based on wide bandgap devices.

Alex Sanchez received the B.Sc. degree in industrial electronics and the M.Sc. degree in energy and power electronics from the University of Mondragón, Mondragón, Spain, in 2016 and 2018, respectively.

Since 2020, he has been with the Ikerlan Technology Research Centre, Mondragón, as a Researcher in power electronics area. His current research interests include the design, optimization, control, and the validation of power converters for inductive power transfer based on wide-bandgap devices and vertical transportation applications.

Alejandro Rujas received the B.Sc. degree in electronics from the University of Mondragón, Mondragón, Spain, in 2004, and the M.Sc. degree in electrical engineering from the Swiss Federal Institute of Technology, Lausanne, Switzerland, in 2007.

Since 2007, he has been with the IK4-Ikerlan Technology Research Centre, Mondragón, as a Researcher in power electronics area. Since 2016, he has also been the Leader of the Power Converter Team, IK4-Ikerlan Technology Research Centre. He has been involved in several industrial and research project related the design and control of power electronics converters for electrical traction, renewable energy, aeronautics, and energy storage applications.